

See discussions, stats, and author profiles for this publication at: <https://www.researchgate.net/publication/235755057>

# $\alpha$ -Fe<sub>2</sub>O<sub>3</sub> Nanocolumns and Nanorods Fabricated by Electron Beam Evaporation for Visible Light Photocatalytic and Antimicrobial Applications

ARTICLE in ACS APPLIED MATERIALS & INTERFACES · FEBRUARY 2013

Impact Factor: 6.72 · DOI: 10.1021/am303017c · Source: PubMed

---

CITATIONS

17

---

READS

69

5 AUTHORS, INCLUDING:



Pradip Basnet

University of Georgia

12 PUBLICATIONS 35 CITATIONS

SEE PROFILE



Ravi Jadeja

University of Georgia

14 PUBLICATIONS 57 CITATIONS

SEE PROFILE

# $\alpha$ -Fe<sub>2</sub>O<sub>3</sub> Nanocolumns and Nanorods Fabricated by Electron Beam Evaporation for Visible Light Photocatalytic and Antimicrobial Applications

Pradip Basnet,<sup>†,||</sup> George K. Larsen,<sup>\*,†,||</sup> Ravirajsinh P. Jadeja,<sup>‡</sup> Yen-Con Hung,<sup>‡</sup> and Yiping Zhao<sup>†</sup>

<sup>†</sup>Department of Physics and Astronomy, and Nanoscale Science and Engineering Center, University of Georgia, Athens, Georgia 30602, United States

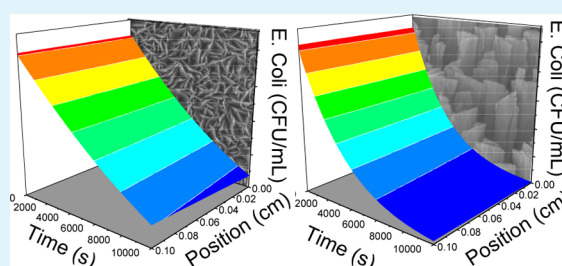
<sup>‡</sup>Department of Food Science and Technology, University of Georgia, Griffin, Georgia 30223, United States

## S Supporting Information

**ABSTRACT:** Both Fe<sub>2</sub>O<sub>3</sub> thin films and nanorod arrays are deposited using electron beam evaporation through normal thin film deposition and oblique angle deposition (OAD) and are characterized structurally, optically, and photocatalytically. The morphologies of the thin films are found to be arrays of very thin and closely packed columnar structures, while the OAD films are well-aligned nanorod arrays. All films were determined to be in the hematite phase ( $\alpha$ -Fe<sub>2</sub>O<sub>3</sub>), as confirmed by both structural and optical characterization. Texture measurements indicate that films have similar growth modes where the [110] direction aligns with the direction of material growth.

Under visible light illumination, the thin film samples were more efficient at photocatalytically degrading methylene blue, while the nanorod arrays were more efficient at inactivating *E. coli* O157:H7. The size of the targeted agent and the different film morphologies result in different reactant/surface interactions, which is the main factor that determines photoactivity. Furthermore, an analytic mathematical model of bacterial inactivation based on chemotactic bacterial diffusion and surface deactivation is developed to quantify and compare the inactivation rate of the samples. These results indicate that  $\alpha$ -Fe<sub>2</sub>O<sub>3</sub> nanorods are promising candidates for antimicrobial applications and are expected to provide insight into the development of better visible-light antimicrobial materials for food products and processing environments, as well as other related applications.

**KEYWORDS:** hematite, *E. coli* O157:H7, [110] orientation, glancing angle deposition, chemotaxis, advection diffusion model



## 1. INTRODUCTION

*Escherichia coli* O157:H7 is a well-known food borne pathogen, responsible for 73,000 illnesses annually and costs the United States approximately \$405 million in medical expenses.<sup>1</sup> *E. coli* O157:H7 infection often leads to bloody diarrhea and hemolytic uremic syndrome (HUS).<sup>2</sup> This pathogen is naturally present in the intestinal tract of cattle; hence the contamination of beef products with bovine feces is the primary source of *E. coli* O157:H7.<sup>3</sup> Besides direct contact with bovine feces, beef products can be contaminated with *E. coli* O157:H7 by coming in contact with contaminated beef processing equipment.<sup>4</sup> Microbial contamination is a serious issue within the food industry. Therefore, there is an urgent need to develop effective antimicrobial agents to help eliminate this pathogen and control its spread in ground beef and beef-processing environments.

The antibacterial agents currently used in the food industry can be classified into two categories: organic and inorganic. The key advantages of inorganic antimicrobial agents over their organic counterparts are improved safety and stability at high temperatures and pressures.<sup>5,6</sup> Therefore, the use of inorganic antimicrobial agents to treat food processing equipment and other food contact surfaces to reduce the chances of cross-

contamination has attracted a lot of attention.<sup>5,7</sup> In particular, photoactivated antimicrobial nanostructures are especially interesting.<sup>6,8,9</sup> These photocatalysts include various oxide semiconducting materials, their metal hybrid nanocomposites, and doped structures such as, TiO<sub>2</sub>, ZnO, CuO, MgO, Ag/TiO<sub>2</sub>, TiO<sub>2</sub>/CuO, TiO<sub>2</sub>/Pt, Au/TiO<sub>2</sub>, Fe<sub>2</sub>O<sub>3</sub>/TiO<sub>2</sub>, and N-, C-, S- doped TiO<sub>2</sub>.<sup>5,6,8–12</sup> Inorganic materials can be used in different forms such as powders, coated on cellulose fibers, or as part of an inorganic/organic nanocomposite coating,<sup>5</sup> and they have been successful in inactivating a wide range of Gram-positive and Gram-negative bacteria.<sup>13</sup>

The dynamics and mechanism of *E. coli* inactivation using photocatalysts under UV, visible light, and solar simulated irradiation have been reported by various studies.<sup>7–9,14</sup> It is believed that the bactericidal effect/killing action is initiated by the photochemical oxidation of intracellular coenzyme A, which alters the respiratory activities.<sup>10,15</sup> However, there is also more direct evidence that the lethal action is due to outer membrane and cell wall damage. This is mainly due to the production of

**Received:** December 7, 2012

**Accepted:** February 28, 2013

**Published:** February 28, 2013

reactive oxygen species (ROS) such as hydroxyl radicals ( $\cdot\text{OH}$ ) and hydrogen peroxide ( $\text{H}_2\text{O}_2$ ) by the photocatalysts under illumination, and can induce phospholipid peroxidation and ultimately lead to cell death.<sup>14</sup>

Of the inorganic antimicrobial agents,  $\text{TiO}_2$  is the most common material used for biocidal application since its first introduction by Matsunaga et al., in 1985. However, the practical use of  $\text{TiO}_2$  nanostructures as a photocatalyst and bactericidal material is limited because of its large band gap ( $E_g = 3.2$  eV,  $\lambda_g = 388$  nm).<sup>11</sup> This means that  $\text{TiO}_2$  photocatalysis is generally unproductive under visible light illumination and can utilize no more than about 2–3% of the incoming solar energy<sup>12</sup> or requires a special UV light source, which is generally harmful to humans. Recently, hematite ( $\alpha\text{-Fe}_2\text{O}_3$ ) has attracted a lot of attention for photocatalytic applications because of its ability to absorb a large part of the solar spectrum ( $E_g = 2.2$  eV,  $\lambda = 564$  nm), its chemical stability (stable through a large pH range), nontoxicity, abundance, and low cost.<sup>16</sup> While magnetite ( $\text{Fe}_3\text{O}_4$ ) and maghemite ( $\gamma\text{-Fe}_2\text{O}_3$ ) have been shown to have antibacterial properties,<sup>17–19</sup>  $\alpha\text{-Fe}_2\text{O}_3$  has not attracted much attention for bactericidal applications, which is surprising because  $\alpha\text{-Fe}_2\text{O}_3$  materials have already been approved by the Food and Drug Administration (FDA) for food and medical applications. The few reports on the antimicrobial properties of hematite have utilized nanoparticle suspensions, and none have described a photoinduced killing mechanism. Sultana et al. detail the antimicrobial effects of nanoparticle solutions of  $\alpha\text{-Fe}_2\text{O}_3$  treated fly ash,<sup>20</sup> while Azam et al. report the inhibition of bacterial growth in  $\alpha\text{-Fe}_2\text{O}_3$  nanoparticle suspensions.<sup>21</sup> The antimicrobial effects of these nanoparticle solutions under ambient laboratory lighting conditions are related to the nanoparticle size effect, where the adsorption of nanoparticles on bacteria adversely affects the permeability of the cell wall.<sup>22,23</sup> Not only would suspended nanoparticle adsorption methods be extremely difficult to implement in industrial settings, the cytotoxicity of such methods could make large scale implementation a public health concern.<sup>24</sup> Thus, an investigation of the photocatalytic and photoinduced biocidal properties of  $\alpha\text{-Fe}_2\text{O}_3$  films is necessary.

Various methods have been used to synthesize  $\alpha\text{-Fe}_2\text{O}_3$  nanostructures, and the photocatalytic behavior of  $\alpha\text{-Fe}_2\text{O}_3$  is strongly dependent on fabrication methods.<sup>25</sup> Physical vapor deposition (PVD) can produce uniform nanostructured thin films, in which the size and geometry can be controlled precisely, and has proven to be a successful method of fabricating uniform, efficient photocatalysts.<sup>26,27</sup> Oblique angle deposition (OAD) is a well-known PVD technique in which the incident material vapor is directed toward a substrate at large incident angles ( $>70^\circ$ ), resulting in the self-organized formation of tilted nanorod arrays due to the shadowing effect.<sup>28</sup> Generally, the nanorods produced by OAD are tilted toward the direction of vapor flux, and the morphology of the individual nanorods is a function of the vapor incident angle and the material properties.<sup>29</sup> The growth is controlled by the geometric shadowing effect and surface diffusion of adatoms. Detailed descriptions of the growth process can be found in some of recent review articles.<sup>30,31</sup> Our group has shown that the photocatalytic behavior of materials depends strongly on morphology of the nanorod arrays, which can be varied by adjusting the deposition parameters.<sup>26</sup> The ability of the OAD method to coat arrays of precisely designed photocatalytic nanostructures onto a wide variety of surfaces without precursors and binders, while being scalable to industrial

production, makes it a suitable platform to investigate  $\alpha\text{-Fe}_2\text{O}_3$  photocatalytic and antimicrobial surfaces.

In this study, both  $\text{Fe}_2\text{O}_3$  thin films and  $\text{Fe}_2\text{O}_3$  OAD nanorod arrays are deposited using electron beam evaporation and are characterized structurally and optically, and are further tested for photocatalytic and antimicrobial applications. The morphologies of the thin films are found to be arrays of very thin and closely packed columnar structures with prismatic ends, while the OAD films are well-aligned nanorod arrays. All films were determined to be in an oriented  $\alpha\text{-Fe}_2\text{O}_3$  phase by X-ray diffraction and Raman spectroscopy. The optical properties of the films are found to be consistent with porous  $\alpha\text{-Fe}_2\text{O}_3$ . We find that the thin films are more photocatalytically active than the nanorod arrays for methylene blue degradation under visible light irradiation, while the nanorod arrays have higher antimicrobial activity under visible light irradiation. The biocidal results are described quantitatively by a mathematical model that is based on chemotactic bacterial diffusion and surface deactivation and are explained qualitatively by the different bacteria adsorption and adherence properties of the two film morphologies, which are especially important parameter for  $\alpha\text{-Fe}_2\text{O}_3$  films because of slow charge transfer kinetics and the relatively low oxidation potential of  $\alpha\text{-Fe}_2\text{O}_3$ .

## 2. EXPERIMENTAL SECTION

**2.1. Materials.** The source material,  $\text{Fe}_2\text{O}_3$  (99.85+%, metal base), was purchased from Alfa Aesar (Ward Hill, MA) and was used as received. Both cleaned glass microscope slides (Gold Seal Catalog No. 3010) and Si (100) wafer (Montco Silicon Technologies Inc.) were used as substrates. High purity Methylene Blue (MB,  $\text{C}_{16}\text{H}_{18}\text{ClN}_3\text{S}$ , Alfa Aesar) aqueous solution was used for photocatalytic activity measurement.

**2.2. Sample Preparation.**  $\text{Fe}_2\text{O}_3$  thin films and nanorods were prepared by a custom designed vacuum deposition system equipped with an electron-beam evaporation source (Torr International, Inc.). The glass substrates were cut into sizes of 9.0 mm  $\times$  27.0 mm and 20.0 mm  $\times$  20.0 mm while Si substrates were cut into size 10.0 mm  $\times$  10.0 mm. Glass substrates were cleaned with a mixture of sulfuric acid ( $\text{H}_2\text{SO}_4$ ) and hydrogen peroxide ( $\text{H}_2\text{O}_2$ ) solution, in a 4:1 ratio, by boiling about 15 min and drying with nitrogen ( $\text{N}_2$ ) flow. Si wafers were cleaned in a mixture solution of deionized (DI) water,  $\text{H}_2\text{O}_2$ , and ammonium hydroxide ( $\text{NH}_4\text{OH}$ ) in the ratio 5:1:1, boiling for 15 min and drying with  $\text{N}_2$  flow. Prior to the deposition, the chamber was evacuated to a pressure less than  $1 \times 10^{-6}$  Torr. During the deposition, the pressure was maintained to about  $\leq 4 \times 10^{-5}$  Torr. For the thin film deposition, the vapor incident angle,  $\theta$ , was set to  $0^\circ$  from the substrate normal. For OAD nanorod growth, the vapor incident angle was set to a large angle, that is,  $\theta = 86^\circ$ . The deposition rate and the deposited thickness were monitored by a quartz crystal microbalance (QCM) positioned directly facing the material vapor flux. The deposition rate was maintained at 0.12 nm/s. For thin film, the final QCM thicknesses reading was 1  $\mu\text{m}$ , while for OAD samples the QCM reading was 2  $\mu\text{m}$ .

After the deposition, some of the as-deposited films and OAD samples were annealed in a quartz tube furnace (Lindberg/Blue M Company, Model Number HTF55347C) under ambient conditions at temperatures  $T = 250$ , 350, and  $450^\circ\text{C}$ , respectively. During annealing, the heating rate was set to  $5^\circ\text{C}$  per minute, ramping up to the desired annealing temperature, and the samples were maintained at the final preset temperature for 4 h.

**2.3. Characterization.** The samples were characterized by a PANalytical X'Pert PRO MRD X-ray diffractometer with fixed incidence angle of  $1.5^\circ$ . The X-ray diffraction (XRD) patterns were recorded with Cu  $K\alpha$  radiation ( $\lambda = 1.5405980$  Å) in the  $2\theta$  range from  $20^\circ$ – $80^\circ$  at a step size of  $0.014^\circ$ . Pole figures were measured using an open Eulerian cradle and poly capillary lens with  $\Delta\theta = 5^\circ$   $\Delta\psi = 5^\circ$ . The OAD nanorod array samples were oriented such that the

tilting direction was pointed toward the X-ray source at  $\theta = 0^\circ$ ,  $\psi = 0^\circ$  for both the  $2\theta$  scans and pole figure measurements. Raman spectroscopy measurements were recorded using a Bruker Senterra Raman microscope, by exciting the samples with a 532 nm wavelength laser at room temperature, with a 10 s exposure time and 1 mW power. The morphologies of the samples were examined by a field-emission scanning electron microscope (SEM) equipped with an energy dispersive X-ray spectroscopy (FEI Inspect F). The optical properties of the samples were measured by a double beam UV–visible light (UV–vis) spectrophotometer (JASCO V-570) over a wavelength range from 200 to 800 nm.

The photocatalytic activities of the samples were evaluated by the photocatalytic degradation of a 10 ppm ( $\sim 31 \mu\text{M}$ ) methylene blue (MB) aqueous solution (pH value  $\sim 6.2$ ) under visible light irradiation. The samples on glass substrates were placed into a 10 mm  $\times$  10 mm  $\times$  45 mm clear methacrylate cuvette filled with 4.0 mL of MB solution. The cuvettes were illuminated by a 250 W quartz halogen lamp (UtiliTech) covering the wavelength range from 400 to 800 nm. The incident light intensity on the sample was kept constant at 65 mW/cm<sup>2</sup> as measured by an optical power meter (Thorlabs PM100D/S310C). A rectangular mask (2.4 cm<sup>2</sup>) was placed in front of the Fe<sub>2</sub>O<sub>3</sub> samples to keep the light power the same for all samples during the photodegradation measurements. A water filter was placed in front of the cuvette to absorb the IR light. The photodegradation of the MB solution was measured by examining the in situ UV–vis transmission spectra of the MB solution using an Ocean Optics spectrophotometer (USB 2000). The time evolution of the absorbance peak at  $\lambda = 664$  nm was used to calculate the photodegradation rate.

**2.4. Bacterial Cultures.** Five strains of *E. coli* O157:H7, E009 (beef), E0122 (cattle), O157-1 (beef), O157-4 (Human), and O157-5 (Human) were used in this study. Strains O157-1 and O15-5 are genetically diverse and from different sources, while other strains were used in numerous previous studies.<sup>32–34</sup> All bacterial strains were stored at  $-70^\circ\text{C}$  in tryptic soy broth (TSB) (Difco, Becton Dickinson, Sparks, MD) containing 20% glycerol. Prior to the experiment, cultures were activated at least twice by growing them overnight in 10 mL of TSB at  $37^\circ\text{C}$ . Cultures were then sedimented three times by centrifugation ( $4,000 \times g$  for 15 min), and the pellets were resuspended in phosphate buffered saline (PBS, pH = 7). At the end of centrifugation, appropriate dilutions were made to achieve a final concentration of  $10^7$  CFU/mL. A bacterial cocktail was prepared by adding 5 mL of each strain to a sterile 50 mL tube. The bacterial population of the cocktail was determined by plating 0.1 mL of the appropriate serial dilution on tryptic soy agar (TSA) (Difco, Becton Dickinson, Sparks, MD). Plates were incubated at  $37^\circ\text{C}$  for 24 h before enumeration.

**2.5. Antimicrobial Efficacy Test.** Fe<sub>2</sub>O<sub>3</sub> thin films and nanorods were sanitized by exposing to a 30 W UV light (Osram Sylvania lighting Inc., Danvers, MA) for 30 min in a biological safety cabinet (Class II Type A/B3, NuAire, Inc., Plymouth, MN). A 100  $\mu\text{L}$  portion of the bacterial cocktail was pipetted onto the surfaces of the Fe<sub>2</sub>O<sub>3</sub> samples. The antibacterial experiments were carried out in a cardboard enclosure at room temperature using a fluorescent light (Model 13 equipped with F13T5 lamps, StockerYale Inc., Salem, NH). The distance between light source and sample surface was set to be 17 cm to keep the intensity fixed at 10 mW/cm<sup>2</sup>. At the end of 30, 60, 120, and 180 min light exposures, bacteria from samples were recovered by placing samples in 10 mL of PBS + 0.1% Tween 80 buffer and vortexing for 30 s. Bacterial enumeration was carried out by plating a 100  $\mu\text{L}$  suspension on TSA and Sorbitol MacConkey agar (SMAC) (Difco, Becton Dickinson, Sparks, MD) in duplicates. Plates were placed in  $37^\circ\text{C}$  for 24 h before bacterial enumeration. Two control experiments were performed, one under illumination using uncoated glass substrates, and the other in the dark using Fe<sub>2</sub>O<sub>3</sub> thin film and nanorod substrates. Neither control experiment exhibited experimentally significant antimicrobial effects.

### 3. RESULTS AND DISCUSSIONS

#### 3.1. Morphology and Structural Characterization.

SEM images were collected to investigate the morphology of the Fe<sub>2</sub>O<sub>3</sub> thin film and nanorod samples. Figures 1a and 1b

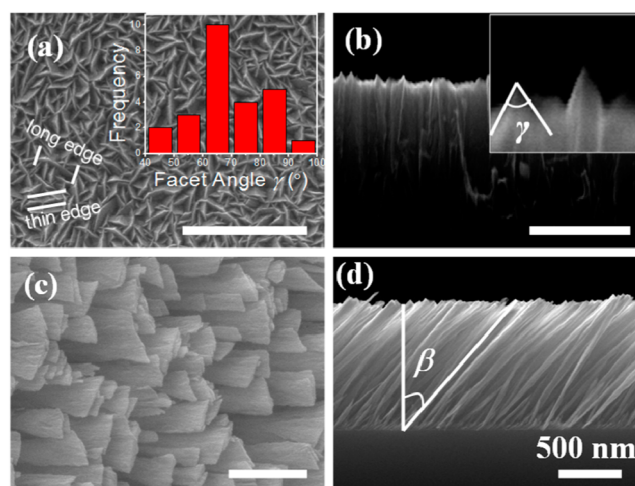


**Figure 1.** SEM micrographs of (a) top-view and (b) cross-sectional view of the as-deposited Fe<sub>2</sub>O<sub>3</sub> thin film, and (c) top-view and (d) cross-sectional view of the as-deposited Fe<sub>2</sub>O<sub>3</sub> OAD nanorod film. Inset in panel (a) shows the histogram of the measured angle between the prismatic facets at the nanocolumn ends, which are defined in the inset in panel (b). The scale bars are all equal to 500 nm.

show representative top and cross-section views of a Fe<sub>2</sub>O<sub>3</sub> thin film. The top view SEM image shows that the Fe<sub>2</sub>O<sub>3</sub> thin films have fine, elongated granular surface features (Figure 1a), while the cross-section SEM image shows that these surface features are the prismatic ends of vertical columnar-like structures (Figure 1b). As measured from the top view SEM image, the thin edge of the surface grain structures have an average width of  $60 \pm 20$  nm, and the long edge has an average length of  $140 \pm 30$  nm. The angles between the prismatic facets,  $\gamma$ , on the top surface of the columns are measured from the cross-section SEM image (inset Figure 1b) and are most frequently found to be between  $60^\circ$ – $70^\circ$  (inset Figure 1a). The morphology of the thin film is interesting and is the result of the preferred orientation of the polycrystalline grains. This will be discussed in more detail below. The thickness of the thin film is determined to be  $920 \pm 20$  nm. The morphological parameters of the thin films are consistent for all samples at different annealing temperatures.

Figures 1c and 1d show the top and cross-section views of the OAD Fe<sub>2</sub>O<sub>3</sub> films, respectively. As expected, the overall morphology of the OAD films is found to be an array of well-aligned tilted nanorods. The nanorods are inclined at angle,  $\beta = 46^\circ \pm 4^\circ$  with respect to the substrate normal, as indicated in Figure 1d. This angle is different than the angle predicted by both the tangent rule ( $\beta = \frac{1}{2} \tan \theta$ )<sup>35</sup> and the cosine rule ( $\beta = \theta - \arcsin(1 - \cos(\theta/2))$ ),<sup>36</sup> which respectively predict  $\beta \approx 82^\circ$  and  $58^\circ$  for the vapor incident angle,  $\theta = 86^\circ$ . Thus, the material dependent model described by Tanto et al. is necessary to explain the tilting angle of the films.<sup>37</sup> They define a material dependent fan-angle,  $\phi$ , such that



for  $\theta \leq \phi$ :

$$\beta = \theta - \arctan \left[ \frac{\sin \phi - \sin(\phi - 2\theta)}{\cos(\phi - 2\theta) + \cos \phi + 2} \right] \quad (1)$$

$$\text{for } \theta \leq \phi: \quad \beta = \theta - \phi/2 \quad (2)$$

Although a more thorough study of the tilting angle versus deposition angle for  $\text{Fe}_2\text{O}_3$  films is necessary for a rigorous result, the measured tilting angle of  $\beta = 46^\circ$  for  $\theta = 86^\circ$  suggests that  $\phi = 80^\circ$ . The average thickness of the OAD films is found to be  $1030 \pm 20$  nm, while the average nanorod length is  $1480 \pm 30$  nm. The diameter of the nanorod increases along the length of the nanorod, with the fanning out of the diameter being greater in the direction perpendicular to the vapor flux. The average diameter at the top of the nanorods in the direction perpendicular to the vapor flux is  $200 \pm 40$  nm, as measured from the top view SEM image. The average diameter of the nanorods in the direction parallel with the vapor flux is  $50 \pm 10$  nm at the bottom,  $60 \pm 10$  nm at the middle, and  $80 \pm 10$  nm at the top, as measured from the cross-sectional SEM image. The nanorod density ( $\eta$ ) was found to be approximately  $10 \pm 2$  rods/ $\mu\text{m}^2$ . Using these parameters, the porosities of the OAD films are estimated to be greater than 64%.

XRD measurements were taken to determine the crystalline phase of the samples. Figures 2a and 2b show the XRD patterns

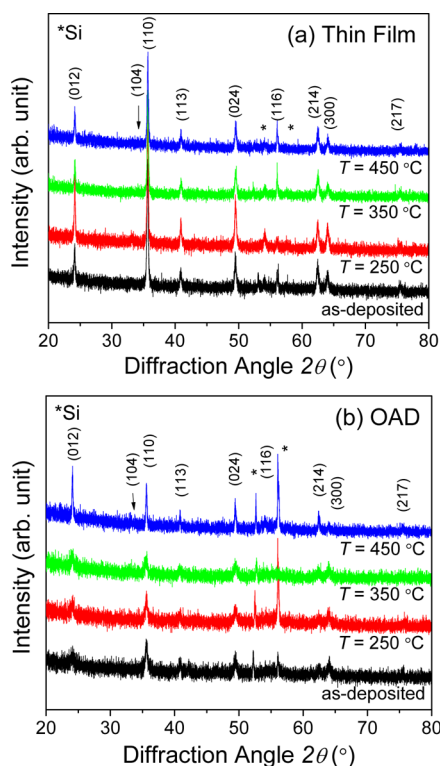


**Figure 2.** XRD spectra with peak attributions of the  $\text{Fe}_2\text{O}_3$  (a) thin films and (b) OAD nanorods deposited on silicon substrates. Note that the spectra have been shifted vertically for clarity.

of the as-deposited and annealed  $\text{Fe}_2\text{O}_3$  thin films and nanorods. Both the thin films and the nanorods are observed to have similar diffraction peak positions, which, as indicated in Figures 2a and 2b, correspond with either the peaks listed for the standard powder diffraction of rhombohedral  $\alpha\text{-Fe}_2\text{O}_3$  (JPCDS No. 00-033-0664) or with peaks associated with the

Si substrate. Thus, all of the films are in the hematite phase. For the thin films, the peak intensities and widths remain mostly constant across annealing temperatures, indicating that the as-deposited films are primarily polycrystalline  $\alpha\text{-Fe}_2\text{O}_3$  with a negligible amount of amorphous regions. For the nanorods, the XRD peak intensities and widths remain mostly constant for annealing temperatures  $T \leq 350$  °C, but at  $T = 450$  °C, a moderate amount of peak sharpening is observed. This peak sharpening is not likely due to grain coarsening since coarsening is not seen in the thin films where it is more energetically favorable.<sup>38</sup> Thus, the peak sharpening indicates that the as-deposited OAD films are polycrystalline  $\alpha\text{-Fe}_2\text{O}_3$  but still contain amorphous regions, and after annealing at  $T = 450$  °C, these amorphous regions begin to transition into the  $\alpha\text{-Fe}_2\text{O}_3$  phase.

To quantify the behavior of crystallite growth, the average grain sizes of  $\alpha\text{-Fe}_2\text{O}_3$  crystallites for the samples are estimated using the Scherrer equation for the {110} and {012} crystal plane reflections and are listed in Table 1. The average

**Table 1.** Average Crystallite Sizes Calculated from the {110} and {012} Diffraction Peaks in the  $\text{Fe}_2\text{O}_3$  Thin Films and Nanorods

sample	thin films		nanorods	
	{110} (nm)	{012} (nm)	{110} (nm)	{012} (nm)
as-deposited	42	83	30	17
$T = 250$ °C	47	69	35	42
$T = 350$ °C	53	69	18	30
$T = 450$ °C	42	83	47	52

crystallite size of the thin films are in the range of 42–53 nm in the [110] direction (note that all crystal orientations are written in the hexagonal  $\{hkl\}$  notation, omitting the redundant index  $i$ ). The estimated crystal sizes in the direction perpendicular to the {012} planes are larger than in the [110] direction and are 83 nm for the as-deposited samples and  $T = 450$  °C samples and 69 nm for the  $T = 250$  °C and  $T = 350$  °C samples. The apparent lack of relationship between annealing temperature and crystallite size agrees well with the supposition that there is a negligible amount of amorphous region in the thin films to feed further grain growth at the higher annealing temperatures. The fluctuations in crystallite size for the different samples could be related to the local environment of the substrate during film growth. The average crystallite sizes of the nanorods are generally smaller than those of the thin films; they are between 30 and 47 nm in the [110] direction and 17–52 nm perpendicular to the {012} planes (Table 1). Aside from the  $T = 350$  °C sample, the crystallite size generally increases with annealing temperature, suggesting that there is grain growth occurring through an amorphous to  $\alpha\text{-Fe}_2\text{O}_3$  transition. The smaller crystallite size in the  $T = 350$  °C sample could be the result of the local environment of that sample during film growth, and that larger grain growth is limited by the absence of coarsening for temperatures  $T \leq 450$  °C. As mentioned above, the columnar structures and prismatic facets observed in the SEM images of the thin films suggest that the  $\text{Fe}_2\text{O}_3$  exhibits a preferential growth direction. In the standard powder diffraction pattern of  $\alpha\text{-Fe}_2\text{O}_3$ , the (104) crystal plane reflection is the most intense, but this reflection is not observed in the XRD spectra of the OAD and thin films. Instead, the most intense reflection for both sets of films, except for the OAD film annealed at  $T = 450$  °C, is the (110) reflection. To better

understand the crystallite orientations of the films, the XRD pole figures for the (110), (012), and (104) reflections were measured for both the thin films and the nanorods deposited on glass substrates and annealed at  $T = 350\text{ }^{\circ}\text{C}$  (Figure 3).

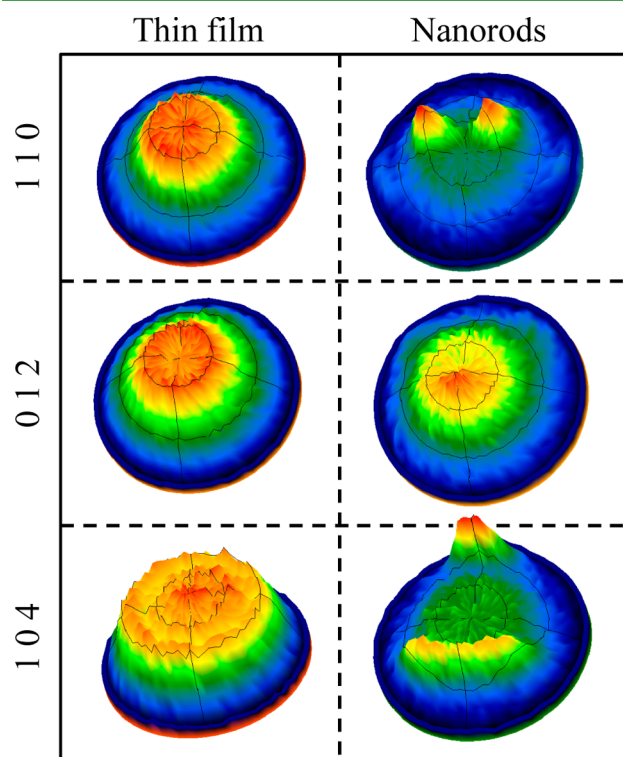


**Figure 3.** Pole figures of the  $\text{Fe}_2\text{O}_3$  thin film and OAD nanorods annealed at  $T = 350\text{ }^{\circ}\text{C}$  for the  $\{110\}$ ,  $\{012\}$ , and  $\{104\}$  crystal plane reflections of  $\alpha\text{-Fe}_2\text{O}_3$ . Note that the nanorod sample was oriented such that the tilting direction was pointed toward the X-ray source at  $\theta = 0^\circ$ ,  $\psi = 0^\circ$ .

Note that the pole figures have not been corrected for background or defocusing. For the thin film, there appears to be a more intense region from  $\psi = 0^\circ$ – $30^\circ$  in all pole figures (Figure 3), which could be due to the background, defocusing, or to a changing orientation as film growth develops. However, it is clear that the (110) pole is centered over  $\psi = 0^\circ$ , the (012) pole forms a ring around  $\psi = 32^\circ$ , and the (104) pole figure has an intensity maximum at  $\psi = 54^\circ$ . These positions are consistent with the  $[110]$  growth direction of  $\alpha\text{-Fe}_2\text{O}_3$ , which would orient the poles of (110), (012), and (104) at  $\psi = 0^\circ$ ,  $\psi = 36^\circ$ , and  $\psi = 56^\circ$ , respectively. The  $[110]$  growth direction is likely responsible for the morphological parameters of the thin films seen in the SEM images. This can be seen in the columnar structures, as the  $\{001\}$  plane is normal to the substrate and is also a cleavage plane of  $\alpha\text{-Fe}_2\text{O}_3$ . The width and length of the prismatic surface features are  $56 \pm 21\text{ nm}$  and  $138 \pm 33\text{ nm}$ , respectively, and scale with the length of the unit axes of  $\alpha\text{-Fe}_2\text{O}_3$ , which are  $a = 5.04\text{ \AA}$  and  $c = 13.76\text{ \AA}$ . The angles between the exposed facets of the prismatic columnar tips are found to be primarily between  $\gamma = 60^\circ$ – $70^\circ$ , which matches well with the inner angle,  $60^\circ$ , between the  $\{110\}$  planes in  $\alpha\text{-Fe}_2\text{O}_3$ .

The pole figures for the (110), (012), and the (104) reflections of the OAD nanorods are shown in Figure 3. The (110) poles of the nanorods are centered over  $\psi = 35^\circ$ , the (012) poles are centered over  $\psi = 10^\circ$ , and the (104) poles are

centered over  $\psi = 47^\circ$  and  $\psi = 73^\circ$ . The orientation of the  $[110]$  direction in the nanorods is tilted away from the substrate normal at  $\psi = 35^\circ$ , but it is not fully aligned with the material growth direction, which is at  $\beta = 46^\circ$ . While the  $[110]$  directions of the thin and OAD films are oriented differently relative to the substrate, both appear to be influenced by the direction of material growth. However, the slight misalignment between the material growth direction and the  $[110]$  direction might contribute to the greater amorphization of the nanorods compared to the thin films. Material growth in the  $[110]$  direction for both films could be the result of oxygen deficiency in the incoming vapor flux. The  $[110]$  direction is Fe-rich, and the  $\{110\}$  planes are relatively Fe-deficient<sup>39</sup> and have among the lowest surface energies of the main faces of  $\alpha\text{-Fe}_2\text{O}_3$  crystallites.<sup>40</sup> It is interesting to note that growth in the  $[110]$  direction appears to be common in hematite nanostructure synthesis and has been seen in nanostructures fabricated by hydrothermal methods,<sup>41</sup> chemical vapor deposition,<sup>42</sup> pulsed laser deposition,<sup>43</sup> and thermal oxidation.<sup>39</sup>

To further confirm crystal phases of the  $\text{Fe}_2\text{O}_3$  films, Raman spectroscopy measurements were carried out for both the as-deposited and the  $T = 450\text{ }^{\circ}\text{C}$  annealed samples. The measured spectra are shown in Figure 4. Each spectrum represents the

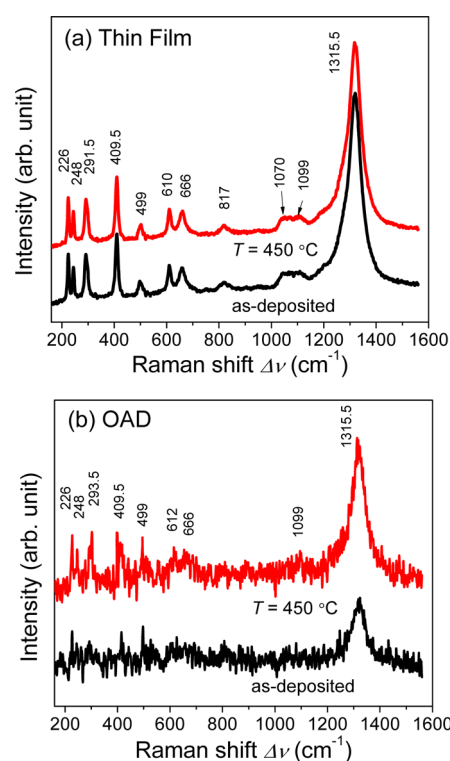


**Figure 4.** Raman spectra of the as-deposited and  $450\text{ }^{\circ}\text{C}$  annealed  $\text{Fe}_2\text{O}_3$  (a) thin films and (b) OAD nanorods. Note that the spectra have been shifted vertically for clarity.

average of three measurements, which were recorded over the detection range from  $\Delta\nu = 200$ – $1600\text{ cm}^{-1}$  at room temperature. Both the thin films and the nanorods are observed to have similar peak positions, although there is a greater noise level in the nanorod samples because of the smaller material volume. For both sets of films, the peak positions do not change after annealing at  $T = 450\text{ }^{\circ}\text{C}$ . Importantly, all of the observed Raman peaks are attributed to  $\alpha\text{-Fe}_2\text{O}_3$ . The peaks at  $\Delta\nu = 226, 248, 292, 410, 499,$  and  $610\text{ cm}^{-1}$  respectively

correspond with the  $A_{1g}$ ,  $E_g$ ,  $E_g$ ,  $E_g$ ,  $A_{1g}$ , and  $E_g$  modes of  $\alpha$ - $\text{Fe}_2\text{O}_3$ .<sup>44</sup> The peak at  $\Delta\nu = 1316\text{ cm}^{-1}$  is attributed to a second order phonon mode of  $\alpha$ - $\text{Fe}_2\text{O}_3$ .<sup>45</sup> The peak appearing at  $\Delta\nu = 666\text{ cm}^{-1}$  is attributed to an IR mode that can manifest in the Raman spectra of  $\alpha$ - $\text{Fe}_2\text{O}_3$  because of the relaxation of Raman selection rules in nanostructured materials.<sup>44</sup> The peak at  $\Delta\nu = 820\text{ cm}^{-1}$  agrees well with the predicted Raman shift due to one magnon scattering.<sup>46</sup> Finally, the smaller peaks at  $\Delta\nu = 1070$  and  $1099\text{ cm}^{-1}$  are consistently seen in the Raman spectra of pure  $\alpha$ - $\text{Fe}_2\text{O}_3$ , but are typically unassigned.<sup>44</sup> Thus, the Raman spectroscopy measurements confirm the XRD results in showing that the films are purely hematite.

**3.2. Optical Properties.** Visual inspection suggests that the appearance of thin films and OAD films are optically similar to  $\alpha$ - $\text{Fe}_2\text{O}_3$ , as both sets of films exhibit the reddish-brown color, typical of hematite (photographic insets Figures 5a and 5b). To

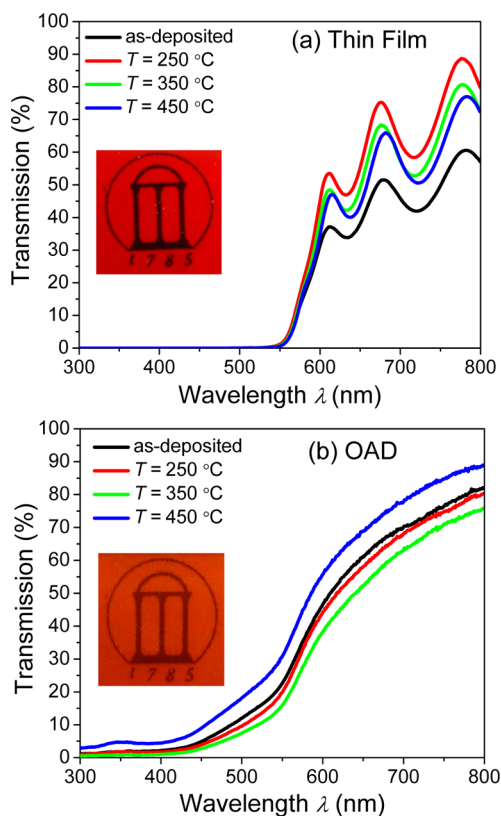


**Figure 5.** Transmission spectra of the  $\text{Fe}_2\text{O}_3$  (a) thin films and (b) OAD nanorods. Insets show a representative photographic image of a (a) thin film and (b) nanorod sample, deposited on glass substrates placed over a University of Georgia logo.

characterize the optical properties of the  $\text{Fe}_2\text{O}_3$  films, the optical transmission spectra were measured by UV–vis spectroscopy and are shown in Figures 5a and 5b. Both sets of films show significant attenuation of visible light beginning around  $\lambda = 600\text{ nm}$ , with the OAD films being more transparent because of their smaller material volume and larger porosity. The interference fringes seen in the spectra of the thin films are not seen in the OAD films because of decoherence from the broadband diffuse scattering of the nanorods. Using the interference fringes, the refractive index and porosity of the  $\text{Fe}_2\text{O}_3$  thin films can be estimated via the envelope method.<sup>47</sup> The refractive index is calculated using

$$n(\lambda) = [N + (N^2 - n_s^2)^{1/2}]^{1/2} \quad (3)$$

$$N(\lambda) = 2n_s \frac{T_{\max} - T_{\min}}{T_{\max} T_{\min}} + \frac{n_s^2 + 1}{2} \quad (4)$$

where  $T_{\max}$  is the transmission given by the maximum envelope function,  $T_{\min}$  is the transmission given by the minimum envelope function, and  $n_s$  is the refractive index of the substrate ( $n_s = 1.52$ , for glass). The film porosity,  $P$ , can be estimated from the index of refraction,  $n$ , using<sup>48</sup>

$$P = \left[ 1 - \frac{n^2 - 1}{n_d^2 - 1} \right] \times 100 \quad (5)$$

where  $n_d = 2.87$  is the pore-free refractive index of  $\alpha$ - $\text{Fe}_2\text{O}_3$  at  $\lambda = 750\text{ nm}$ . The results are summarized in Table 2. As expected,

**Table 2.** Derived Optical Parameters of the  $\text{Fe}_2\text{O}_3$  Thin Films and Nanorods

sample	thin films			nanorods
	refractive index at 750 nm	porosity (%)	band gap (eV)	band gap (eV)
as-deposited	2.49	28.1	2.21	2.09
$T = 250\text{ }^\circ\text{C}$	2.36	36.9	2.19	2.08
$T = 350\text{ }^\circ\text{C}$	2.26	43.2	2.17	2.07
$T = 450\text{ }^\circ\text{C}$	2.46	30.2	2.17	2.11

the refractive indices of the thin films are less than the literature value because of the nanocolumnar morphology. The porosities of the thin films vary, with the as-deposited film being the least porous with 28% void and the  $T = 350\text{ }^\circ\text{C}$  film being the most porous with 43% void. The porosity of the thin film scales with the estimated crystallite size in the direction perpendicular to the  $\{012\}$  planes and not with the crystallite size in the  $[110]$  direction. This observation is consistent with the preferred orientation of the  $\text{Fe}_2\text{O}_3$  thin films seen in the XRD analysis and with the supposition that the columnar morphology is primarily responsible for the porosity in the thin films. The varying porosities are not expected to be the result of the annealing treatment; instead, they are likely the result of different local environments during film growth.

The optical absorption coefficient  $\alpha(\lambda)$  is calculated, assuming reflection is negligible, from the experimentally measured transmittance data,  $T(\lambda)$ , using the relation:<sup>49</sup>  $\alpha(\lambda) = 1/d \ln(1/T)$ , where  $d$  denotes the film thickness. The absorption coefficient is used to estimate the apparent band gap energy,  $E_g$ , of the samples utilizing the Tauc relation:  $(\alpha h\nu) \propto (h\nu - E_g)^{1/2}$ , since  $\alpha$ - $\text{Fe}_2\text{O}_3$  is a direct band gap material. By plotting  $(\alpha h\nu)^2$  versus  $h\nu$  and extrapolating the linear portion of the curve back to the abscissa, the optical band gap can be estimated. The Tauc plot analyses for the  $\text{Fe}_2\text{O}_3$  thin films and nanorods are summarized in Table 2. For the thin films,  $E_g = 2.17$ – $2.21\text{ eV}$ , while for the nanorods  $E_g = 2.07$ – $2.11\text{ eV}$ . The band gap energies are similar within each set of samples, but the extrapolated band gaps of the nanorods are less than the thin films. This is likely due to the increased diffuse scattering of the OAD nanorods at longer wavelengths, but also could be attributed to a wider Urbach tail. However, these results agree fairly well with previously reported results for the hematite band gap,  $E_g = 2.1$ – $2.7\text{ eV}$ .<sup>50</sup>

**3.3. Photocatalytic Activity.** The photocatalytic properties of the  $\text{Fe}_2\text{O}_3$  thin films and OAD films were characterized



using MB photodegradation experiments under visible light illumination. As a control, the absorbance peak of the MB solution was monitored over several hours under two different conditions: (i) with a photocatalyst in the dark and (ii) with a bare glass substrate under visible light illumination. The change in the absorbance peak of MB under these conditions is found to be negligible, indicating that there is no loss of MB without an irradiated photocatalyst. For all  $\text{Fe}_2\text{O}_3$  samples placed in MB solution and under visible light illumination, the MB absorbance peak is observed to decrease with time, indicating the decomposition of MB (Figure 6). The change in the

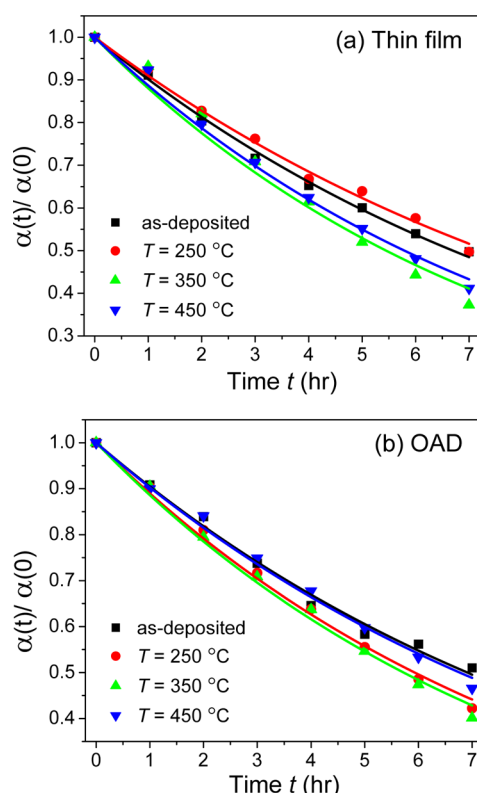


**Figure 6.** Normalized MB absorbance intensities of the  $\lambda = 664$  nm peak versus time for the  $\text{Fe}_2\text{O}_3$  (a) thin films and (b) OAD nanorods. The curves correspond to the first-order exponential decay fittings of the data points, from which the decay rate,  $\kappa$ , was determined.

intensity of the MB absorbance peak at  $\lambda = 664$  nm versus time for all samples exhibits exponential decay behavior. To quantify the results, the MB absorbance peak intensity is normalized to the initial absorbance at  $t = 0$ , and the data are fit to a first-order exponential decay equation,

$$\alpha(t) = \alpha_0 e^{-\kappa_c t} \quad (6)$$

where  $\alpha_0$  is the initial MB absorbance intensity at  $t = 0$  h,  $t$  is time, and  $\kappa_c$  is the decay constant. The fitting results are shown

in Figure 6 as solid curves, and the rate constants,  $\kappa_c$ , for different samples are summarized in Table 3. For the thin films, the samples annealed at the higher temperatures are more efficient photocatalysts, with the sample annealed at  $T = 350$  °C showing the highest decay rate at  $\kappa_c = 0.127 \pm 0.005$   $\text{h}^{-1}$ . The slowest decay rate of all samples is the thin film annealed at  $T = 250$  °C, which has a decay rate of  $\kappa_c = 0.095 \pm 0.002$   $\text{h}^{-1}$ . The decay rates of the nanorods are not a monotonic function of annealing temperature and are similar in value to the decay rates of thin films and range from  $\kappa_c = 0.100$ – $0.121$   $\text{h}^{-1}$ . While it is difficult to compare the results from different MB degradation experiments because of different experimental parameters and setups, it is worthwhile to note that the MB decay rates measured for the  $\text{Fe}_2\text{O}_3$  samples are slower than some decay rates measured by other groups. For example, Zhang et al. found that  $\alpha\text{-Fe}_2\text{O}_3$  nanotube electrodes fabricated by sonoelectrochemical anodization under  $100$   $\text{mW}/\text{cm}^2$  white light illumination exhibited a decay rate of  $\kappa_c = 0.96$   $\text{h}^{-1}$  in a  $1$   $\mu\text{M}$  MB solution.<sup>51</sup> Also, hydrothermally prepared  $\alpha\text{-Fe}_2\text{O}_3$  nanorods ( $0.2$   $\text{mg}/\text{mL}$ ) have been shown to exhibit a decay rate of  $\kappa_c = 0.64$   $\text{h}^{-1}$  under visible light illumination in a  $10$   $\mu\text{M}$  MB solution.<sup>52</sup> Because of the difficulty in comparing results from other groups and experiments, we also fabricated  $\alpha\text{-Fe}_2\text{O}_3$  nanoparticles by coprecipitation and purchased commercially available  $\alpha\text{-Fe}_2\text{O}_3$  nanoparticles to compare with the results for the nanorods and thin films. We found that the coprecipitated nanoparticle MB photodegradation rate,  $\kappa_c = 0.055 \pm 0.002$   $\text{h}^{-1}$ , was less than half the rate of the nanorods and thin films, while the commercial nanoparticles were twice as efficient with  $\kappa_c = 0.211 \pm 0.011$   $\text{h}^{-1}$ , under similar experimental conditions and for roughly the same amount of photocatalytic material,  $0.6$   $\text{mg}$  (see Supporting Information for  $\alpha\text{-Fe}_2\text{O}_3$  nanoparticle photocatalytic experimental details and results). Thus, the nanorods and thin films do outperform  $\alpha\text{-Fe}_2\text{O}_3$  nanoparticle solutions we synthesized using wet chemistry, but are not as efficient as commercially available  $\alpha\text{-Fe}_2\text{O}_3$  nanoparticles in solution. However, there are irreparable intrinsic differences between experiments conducted using photocatalytic thin films and those conducted using nanoparticle solutions, so a comparison between the two different geometries is problematic. The specific application will determine the most suitable photocatalyst structure. Finally, it is interesting to note that the photodecay rates of the nanorods are slightly smaller than those of the thin films, even though the nanorods have a larger porosity.

Effective photocatalysts are films that exhibit efficient charge transfer to and across the semiconductor-solution interface. The annealing process generally increases crystallite sizes and passivates defects, such as oxygen vacancies, improving charge lifetimes. This is why the catalytic efficiency, for the most part, increases with annealing temperature for both the OAD and thin film samples. However, defects can be beneficial by acting as catalytic hot spots and increasing the conductivity of the

**Table 3.** Photocatalytic Decay Rates,  $\kappa_c$ , and Bacterial Inactivation Rates,  $\kappa_b$ , of the  $\text{Fe}_2\text{O}_3$  Thin Films and Nanorods

sample	methylene blue, $\kappa_c$ ( $\text{hr}^{-1}$ )		<i>E. coli</i> O157:H7 $\kappa_b$ ( $\text{cm}/\text{s}$ )	
	thin film	nanorods	thin film	nanorods
as-deposited	$0.103 \pm 0.001$	$0.100 \pm 0.002$	$1.2 \times 10^4$	$4.6 \times 10^4$
$T = 250$ °C	$0.095 \pm 0.002$	$0.117 \pm 0.002$		
$T = 350$ °C	$0.127 \pm 0.005$	$0.121 \pm 0.003$	$1.5 \times 10^4$	$4.8 \times 10^4$
$T = 450$ °C	$0.120 \pm 0.003$	$0.102 \pm 0.002$		



material; thus, the removal of too many defects might explain the decrease in catalytic efficiency at the highest annealing temperature for both the OAD and thin films. It is well-known that  $\alpha$ -Fe<sub>2</sub>O<sub>3</sub> has anisotropic charge transport properties. In particular, the conductivity in the [110] direction, or within the (001) plane, is known to be up to four magnitudes higher than in directions orthogonal to it.<sup>53</sup> Thus, the preferred orientation of the Fe<sub>2</sub>O<sub>3</sub>, as described above, could create an environment favorable for increased charge separation because of the larger crystalline sizes in the more conductive [110] direction, resulting in less grain boundary scattering and trapping of free charges.

However, in addition to efficient charge transfer within the nanostructure, charge transfer across the nanostructure-solution interface is equally important. As mentioned above,  $\alpha$ -Fe<sub>2</sub>O<sub>3</sub> is known to have slow kinetics at aqueous interfaces, but specific crystal planes have been found to be more reactive for certain photocatalytic and catalytic reactions. Gao et al. concluded that  $\alpha$ -Fe<sub>2</sub>O<sub>3</sub> nanorods were more efficient for CO oxidation than  $\alpha$ -Fe<sub>2</sub>O<sub>3</sub> nanotubes and nanocubes because of their greater area of exposed {110} planes.<sup>54</sup> Similar results regarding the greater efficiency of {110} planes for CO oxidation have been reported elsewhere in the literature.<sup>55,56</sup> The explanation for the greater efficiency of {110} planes is that CO adsorbs first to Fe atoms and then is subsequently oxidized by a neighboring surface O atom. Since {110} planes have a large number of surface Fe atoms, more CO is adsorbed and oxidized there.<sup>57</sup> Similarly, Weiss et al. found that cationic Fe sites on the (001) surface were fundamentally important during the catalytic decomposition of ethylbenzene and styrene because of greater reactant adsorbance at these sites, and they postulate a general rule that the chemisorption reactivity of metal oxides requires the presence of acidic metal sites at the surface.<sup>58</sup> Finally, Zhou et al. found that the visible light photodegradation rate of rhodamine B by hematite nanoparticles in the presence of H<sub>2</sub>O<sub>2</sub> strongly depended on the exposed facets of the hematite nanoparticles, when normalized to exposed surface area.<sup>59</sup> In particular, they found that the reactivity of different exposed planes obeyed the relationship, {110} > {012} ≫ {001}. While the photocatalytic and catalytic reactions mentioned above are different than the MB degradation experiment described here, it is clear that reactant adsorption at active Fe surface sites is a critically important factor in determining the efficiency of  $\alpha$ -Fe<sub>2</sub>O<sub>3</sub> photocatalysts. Direct adsorption to a reactive  $\alpha$ -Fe<sub>2</sub>O<sub>3</sub> surface is especially important given the slow charge-transfer kinetics of hematite within the bulk and at interfaces. Furthermore, the reactant must be directly oxidized because the valence band of  $\alpha$ -Fe<sub>2</sub>O<sub>3</sub> is not sufficiently positive to generate hydroxyl radicals (at pH = 7), nor is the conduction band sufficiently negative to generate superoxides,<sup>60,61</sup> which precludes oxidation at a distance via reactive oxygen species and requires direct contact of the reactant with the surface. Thus, it is likely that the exposed crystal planes of the Fe<sub>2</sub>O<sub>3</sub> thin film provide more reactive adsorbance sites for MB molecules, which leads to the slightly higher photocatalytic efficiency of the thin films relative to the OAD films, even though the OAD films are more porous and have a higher surface area.

**3.4. Antimicrobial Activity.** The visible light induced antimicrobial activities of the Fe<sub>2</sub>O<sub>3</sub> thin films and nanorods against *E. coli* O157:H7 were measured and compared. For the biocidal experiment, only the as-deposited and  $T = 350$  °C samples were compared, as these represent the samples with the lowest and highest measured photocatalytic efficiencies,

respectively. The results of the experiment are summarized in Figures 7a and 7b. It is observed that the bactericidal efficacies

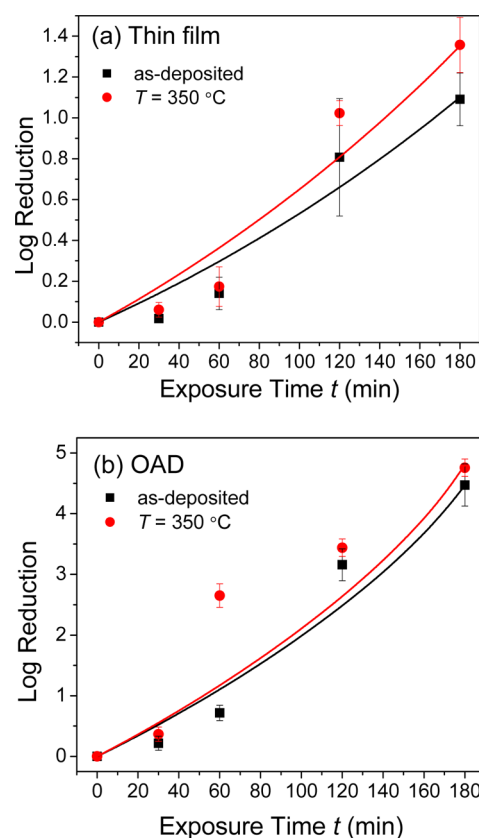


**Figure 7.** Log reduction of *E. coli* O157:H7 as a function of irradiation time for the as-deposited and  $T = 350$  °C Fe<sub>2</sub>O<sub>3</sub> (a) thin films and (b) OAD nanorods. The solid curves are the chemotaxis model fits for the log reduction.

of the nanorod samples are much higher than the thin film samples. The as-deposited and  $T = 350$  °C thin films show 1.1 and 1.5 log reductions in bacteria over 3 h, respectively, while the as-deposited and  $T = 350$  °C nanorod samples are exponentially more efficient, showing log reductions of 4.6 and 4.9 over 3 h, respectively. It is difficult to compare these antimicrobial efficacy results with results from the literature because of large variations in reported experimental parameters such as initial bacteria concentration and strains, illumination intensity and wavelength range, substrate size, and so forth. Additionally, most antimicrobial tests of TiO<sub>2</sub> are conducted using UV light, while the Fe<sub>2</sub>O<sub>3</sub> samples in this experiment were tested using visible light. However, it is worth noting that the log reductions of the nanorod samples compare favorably with results published in the literature for the photocatalytic inactivation of *E. coli* using state of the art TiO<sub>2</sub>-based coatings, which have reported log reductions that range from ~3 to ~5 over 3 h in recent experiments,<sup>62–65</sup> and also compare favorably with other photocatalytic materials such as sphalerite<sup>66</sup> and bismuth vanadate nanotubes,<sup>67</sup> both of which were recently reported to have log reductions of *E. coli* of ~2.5 over 3 h. Furthermore, hematite is the most stable form of iron oxide and should maintain its efficacy over time. Indeed, uncleaned as-deposited Fe<sub>2</sub>O<sub>3</sub> nanorod samples stored in a Petri dish and exposed to open air for longer than 6 months still exhibited a log reduction of 0.29 after 4 h (see Supporting Information for

plot and further discussion). Thus, these initial results indicate that the Fe<sub>2</sub>O<sub>3</sub> nanorods are promising candidates for antimicrobial applications, especially given the intrinsic benefits of  $\alpha$ -Fe<sub>2</sub>O<sub>3</sub> such as low cost, abundance, nontoxicity, visible light utilization, and FDA approval for food and medical applications.

The time dependent biocidal effect of a coated photocatalyst surface has not been well understood, though there are numerous models for suspended nanoparticle/biocidal solutions.<sup>68–71</sup> It is necessary to develop a physical model of the antimicrobial experiment to quantify the bacterial inactivation rate of the samples. We believe that this system can be described by diffusive transport combined with a reactive boundary condition. The one-dimensional chemotaxis diffusion equation is given by<sup>72</sup>

$$\frac{\partial b}{\partial t} = -\frac{\partial}{\partial x} \left( -D \frac{\partial b}{\partial x} + \chi b \frac{\partial c}{\partial x} \right) \quad (7)$$

where  $b(x, t)$  is the bacteria concentration,  $D$  is the bacteria diffusion coefficient,  $\chi$  is the chemotactic sensitivity coefficient, and  $c(x, t)$  is the chemoattractant concentration. If we assume that both  $D$  and  $\chi$  are constant throughout the experiment and the chemoattractant gradient has no curvature, that is,  $\partial^2 c / \partial x^2 = 0$ , eq 7 reduces to the one-dimensional advection equation for  $b(x, t)$ ,

$$\frac{\partial b}{\partial t} = D \frac{\partial^2 b}{\partial x^2} - \chi^* \frac{\partial b}{\partial x} \quad (8)$$

where  $\chi^*$  is the chemotactic sensitivity coefficient that has been modified by the chemoattractant gradient. The two boundary conditions are,

$$\left. \frac{\partial b}{\partial x} \right|_{x=0} = 0 \quad (9)$$

$$\left. \frac{\partial b}{\partial x} \right|_{x=L} = -\frac{\kappa_b}{D} b(x=L, t) \quad (10)$$

where  $L$  is distance from the solution/ambient interface ( $x = 0$ ) to the solution/Fe<sub>2</sub>O<sub>3</sub> interface ( $x = L$ ), and  $\kappa_b$  is the bacterial inactivation rate of the sample. Equation 10 defines the biocidal effect of the surface. Thus, the major assumptions of this model are as follows: the motional behavior of *E. coli* O157:H7 in an aqueous environment that is supported by a Fe<sub>2</sub>O<sub>3</sub> film can be described by a one-dimensional chemotaxis equation; the volume of the aqueous environment does not change appreciably with time; bacteria cannot escape from ambient/solution interface; and bacteria are inactivated by the Fe<sub>2</sub>O<sub>3</sub> film at a rate that is proportional to the bacteria concentration at the solution/Fe<sub>2</sub>O<sub>3</sub> interface. Using the two boundary conditions, eq 9 and eq 10, and the initial condition that  $b(x, t = 0) = b_0$ , the solution to eq 8 is given by (see Supporting Information, for full derivation)

$$b(\xi, t) = \sum_{n=1}^{\infty} c_n e^{-D \lambda_n^2 t} \cos(\lambda_n \xi) \quad (11)$$

$$\xi = x - \chi^* t \quad (12)$$

$$\lambda_n = \frac{\kappa_b}{D} \cot \lambda_n L \quad (13)$$

$$c_n = \frac{2b_0 \lambda_n \sin \lambda_n L}{\lambda_n^2 L + \lambda_n \sin \lambda_n L \cos \lambda_n L} \quad (14)$$

The experiment was modeled using the following values for the parameters:  $n = 50$ ;  $b_0 = 10^7$  CFU/mL;  $L = 0.1$  cm;  $D = 2.6 \times 10^{-5}$  cm<sup>2</sup>/s (average of Table 2 from Lewus and Ford);<sup>73</sup>  $\chi^* = 4 \times 10^{-5}$  cm<sup>2</sup>/s (10% of average of Table 3 from Lewus and Ford).<sup>73</sup> The bacterial inactivation rate,  $\kappa_b$ , was varied until the predicted curve matched the experimental datum at  $t = 180$  min. The results for  $\kappa_b$  range from  $\kappa_b = 1.2 \times 10^4$  cm/s for the as-deposited thin film sample to  $\kappa_b = 4.8 \times 10^4$  cm/s for the nanorod sample annealed at  $T = 350$  °C; a summary is shown in Table 3 and the resulting curves are plotted in Figures 7a and 7b. The model and parameters predict a nonlinear curve for the log reduction, and the agreement between the model and experimental data is reasonably good given the assumed values of  $D$  and  $\chi^*$  and the approximations made during the derivation (see Supporting Information). Experimentally determined values of  $D$  and  $\chi^*$  could improve the quality of the fitting.

The slight increase in bacterial inactivation rate for both sets of films after annealing is unsurprising. However, the superior performance of the nanorods relative to the thin films is surprising, especially given the results from the photocatalytic experiment, where the thin films are found to be slightly more efficient than the nanorod samples. While the degradation pathways for both MB and *E. coli* O157:H7 rely on the oxidation processes, the physical sizes of MB ( $\sim 1$  nm) and *E. coli* O157:H7 ( $\sim 1$   $\mu$ m) are different. Thus, the MB molecule can reach all of the exposed surfaces of the plate-like structures of the thin films and the nanorods of the OAD films, but *E. coli* O157:H7 is much larger than the lateral spacing of the thin films and nanorods and is, therefore, confined to the top surfaces of each film. As described above, direct contact with the Fe<sub>2</sub>O<sub>3</sub> surface is extremely important for oxidative processes given the slow aqueous kinetics and the relatively low oxidation potential of the Fe<sub>2</sub>O<sub>3</sub> films. Furthermore, it has been shown that the rate of adsorption of *E. coli* on a photocatalyst's surface is positively correlated with its bactericidal effect.<sup>74</sup> Thus, it is clear that the ways in which *E. coli* O157:H7 adheres and interacts with the top surfaces of the thin films and nanorods determine their relative efficacy for antimicrobial applications. Further studies are underway to characterize the differences between the behaviors of bacterial adhesion to nanorods and thin films. However, given the greater biocidal effects of the nanorod samples, it is expected that the nanorod array morphology promotes longer contact times of *E. coli* O157:H7 with the Fe<sub>2</sub>O<sub>3</sub> surface, while the bacteria should show an aversion to the prismatic ends of the thin film surface. The greater contact time with the  $\alpha$ -Fe<sub>2</sub>O<sub>3</sub> surface increase the likelihood that *E. coli* O157:H7 can be inactivated via the direct photochemical oxidation of intracellular coenzyme A.<sup>10,15</sup>

The effects of surface properties on cell adhesion are still not well understood and are currently a hot topic in the literature. While no single theory has been established, surface energy, roughness, and zeta potential have been determined to be important factors governing the adhesion strength of bacteria, but the relative importance of the surface properties varies between experiments.<sup>75,76</sup> To compare the surface energies of the films, the contact angle of a deionized water droplet on the Fe<sub>2</sub>O<sub>3</sub> thin films and nanorod samples were measured and were found to be 56.5° and 23.5°, respectively. Thus, either *E. coli* O157:H7 shows a preference for the more hydrophilic surface of the nanorod film or that surface wettability is not an

important parameter in this case. More likely, the surface morphology plays a greater role. It is difficult for the bacteria to conform to the very sharp surface features of the thin film, and, as described by Emerson et al., this inability prevents strong adhesion to the surface.<sup>76</sup> On the other hand, *E. coli* O157:H7 can conform more easily to the smoother edges and larger scale roughness of the top surface of the nanorods, promoting greater adhesion and longer contact times, and allowing more bacteria to be inactivated. To further confirm the dramatic effect that surface morphology has on the photoinduced bactericidal properties of  $\alpha$ -Fe<sub>2</sub>O<sub>3</sub>, the antimicrobial effects of  $\alpha$ -Fe<sub>2</sub>O<sub>3</sub> nanoparticle solutions, using both commercial and coprecipitated nanoparticles we synthesized, were also tested and were found to have negligible antimicrobial properties (see Supporting Information for hematite nanoparticle antimicrobial experimental details and results). Thus, it is clear that the surface morphology of Fe<sub>2</sub>O<sub>3</sub> appears to be an important effect on photoinduced bactericidal efficacy.

#### 4. CONCLUSIONS

We have demonstrated that both Fe<sub>2</sub>O<sub>3</sub> thin films and Fe<sub>2</sub>O<sub>3</sub> nanorod arrays fabricated by electron beam evaporation are purely hematite ( $\alpha$ -Fe<sub>2</sub>O<sub>3</sub>) using structural and optical methods. The thin films were found to be oriented nanocolumnar  $\alpha$ -Fe<sub>2</sub>O<sub>3</sub> with exposed {110} and {001} planes, and the OAD films were found to be arrays of oriented  $\alpha$ -Fe<sub>2</sub>O<sub>3</sub> nanorods. Furthermore, the Fe<sub>2</sub>O<sub>3</sub> thin films and Fe<sub>2</sub>O<sub>3</sub> nanorods were found to be photocatalytically and antimicrobially active under visible light illumination. However, the different morphologies of the films (prismatic nanocolumn versus nanorod) and the different nature of the reactants (organic dye,  $\sim 1$  nm, versus bacteria,  $\sim 1$   $\mu$ m) highlighted how adsorbate/surface interactions are an important consideration for photocatalytic and antimicrobial applications of  $\alpha$ -Fe<sub>2</sub>O<sub>3</sub> films. Specifically, adsorbance of molecular reactants and strong adhesion of bacteria to active surface sites are required to maximize photoinduced degradation. A chemotactic mathematical model of bacterial inactivation was developed to quantify the antimicrobial efficiency of surface coatings. These results are important considerations for future designs of  $\alpha$ -Fe<sub>2</sub>O<sub>3</sub> antimicrobial coatings for the inactivation of *E. coli* O157:H7. It is also important to note, that depending on the specific environment, the nanorod morphology will have some unique challenges if transitioned from the laboratory to an industrial setting. Nanostructures will have to be designed to accommodate the specific environment, which might compromise the antibacterial performance. However, this is true for any antibacterial agent working in a complicated environment where there could be interference at the bacteria/structure interface. Further experiments are underway to investigate how the morphology of electron beam evaporated  $\alpha$ -Fe<sub>2</sub>O<sub>3</sub> can be tuned to optimize bacterial contact with the photocatalytic surface to maximize its biocidal effects.

#### ■ ASSOCIATED CONTENT

##### Supporting Information

SI. Derivation of chemotactic bacteria inactivation model; SII. Long-term stability and antimicrobial efficacy test; SIII. Comparison with hematite nanoparticles ( $\alpha$ -Fe<sub>2</sub>O<sub>3</sub> NPs). This material is available free of charge via the Internet at <http://pubs.acs.org>.

#### ■ AUTHOR INFORMATION

##### Corresponding Author

\*E-mail: [georgelarsen@physast.uga.edu](mailto:georgelarsen@physast.uga.edu).

##### Author Contributions

<sup>||</sup>These authors contributed equally.

##### Notes

The authors declare no competing financial interest.

#### ■ ACKNOWLEDGMENTS

Funding for this study was provided by State and Hatch funds allocated to the University of Georgia Agricultural Experiment Station, Griffin Campus and an Agriculture and food Research initiative Grant 2011-68003-30012 from the USDA National Institute of Food and Agriculture, Food Safety: Food Processing Technologies to Destroy Food-borne Pathogens Program-(A4131). G.K.L. was supported by the National Science Foundation under the contract number ECCS-1029609. The authors would like to thank Dr. J. P. Singh for measuring the Raman spectra.

#### ■ REFERENCES

- (1) Frenzen, P. D.; Drake, A.; Angulo, F. J.; *Emerging Infections*, P. J. *Food Prot.* **2005**, *68*, 2623–2630.
- (2) Andreoli, S. P.; Trachtman, H.; Acheson, D. W. K.; Siegler, R. L.; Obrig, T. G. *Pediatr. Nephrol.* **2002**, *17*, 293–298.
- (3) Rodriguez, A.; McLandsborough, L. A. *J. Food Prot.* **2007**, *70*, 600–606.
- (4) Tuttle, J.; Gomez, T.; Doyle, M. P.; Wells, J. G.; Zhao, T.; Tauxe, R. V.; Griffin, P. M. *Epidemiol. Infect.* **1999**, *122*, 185–192.
- (5) Sawai, J. J. *Microbiol. Methods* **2003**, *54*, 177–182.
- (6) Fu, G. F.; Vary, P. S.; Lin, C. T. *J. Phys. Chem. B* **2005**, *109*, 8889–8898.
- (7) Maness, P. C.; Smolinski, S.; Blake, D. M.; Huang, Z.; Wolfrum, E. J.; Jacoby, W. A. *Appl. Environ. Microbiol.* **1999**, *65*, 4094–4098.
- (8) Li, Q. L.; Mahendra, S.; Lyon, D. Y.; Brunet, L.; Liga, M. V.; Li, D.; Alvarez, P. J. J. *Water Res.* **2008**, *42*, 4591–4602.
- (9) Liou, J. W.; Chang, H. H. *Arch. Immunol. Ther. Exp. (Warsz.)* **2012**, *1*–9.
- (10) Matsunaga, T.; Tomoda, R.; Nakajima, T.; Wake, H. *FEMS Microbiol. Lett.* **1985**, *29*, 211–214.
- (11) Hoffmann, M. R.; Martin, S. T.; Choi, W. Y.; Bahnemann, D. W. *Chem. Rev.* **1995**, *95*, 69–96.
- (12) Sakthivel, S.; Janczarek, M.; Kisch, H. J. *Phys. Chem. B* **2004**, *108*, 19384–19387.
- (13) Foster, H. A.; Ditta, I. B.; Varghese, S.; Steele, A. *Appl. Microbiol. Biotechnol.* **2011**, *90*, 1847–1868.
- (14) Sunada, K.; Watanabe, T.; Hashimoto, K. *J. Photochem. Photobiol. A* **2003**, *156*, 227–233.
- (15) Matsunaga, T.; Tomoda, R.; Nakajima, T.; Nakamura, N.; Komine, T. *Appl. Environ. Microbiol.* **1988**, *54*, 1330–1333.
- (16) Cesar, I.; Kay, A.; Gonzalez Martinez, J. A.; Grätzel, M. *J. Am. Chem. Soc.* **2006**, *128*, 4582–4583.
- (17) Tran, N.; Mir, A.; Mallik, D.; Sinha, A.; Nayar, S.; Webster, T. J. *Int. J. Nanomed.* **2010**, *5*, 277.
- (18) Kong, H.; Song, J.; Jang, J. *Chem. Commun.* **2010**, *46*, 6735–6737.
- (19) Chen, T.; Wang, R.; Xu, L. Q.; Neoh, K. G.; Kang, E.-T. *Ind. Eng. Chem. Res.* **2012**, *51*, 13164–13172.
- (20) Sultana, P.; Das, S.; Bhattacharya, A.; Basu, R.; Nandy, P. *Mater. Sci. Eng., C* **2012**, *32*, 1358–1365.
- (21) Azam, A.; Ahmed, A. S.; Oves, M.; Khan, M. S.; Habib, S. S.; Memic, A. *Int. J. Nanomed.* **2012**, *7*, 6003.
- (22) Zhang, W.; Rittmann, B.; Chen, Y. *Environ. Sci. Technol.* **2011**, *45*, 2172–2178.
- (23) Zhang, W.; Hughes, J.; Chen, Y. *Appl. Environ. Microbiol.* **2012**, *78*, 3905–3915.



- (24) Lewinski, N.; Colvin, V.; Drezek, R. *Small* **2007**, *4*, 26–49.
- (25) Chernyshova, I. V.; Hochella, M. F.; Madden, A. S. *Phys. Chem. Chem. Phys.* **2007**, *9*, 1736–1750.
- (26) Smith, W.; Ingram, W.; Zhao, Y. P. *Chem. Phys. Lett.* **2009**, *479*, 270–273.
- (27) Smith, W.; Zhao, Y. P. *J. Phys. Chem. C* **2008**, *112*, 19635–19641.
- (28) Ye, D. X.; Zhao, Y. P.; Yang, G. R.; Zhao, Y. G.; Wang, G. C.; Lu, T. M. *Nanotechnology* **2002**, *13*, 615–618.
- (29) Robbie, K.; Sit, J.; Brett, M. J. *Vac. Sci. Technol. B* **1998**, *16*, 1115–1122.
- (30) Zhao, Y.; Ye, D.; Wang, G.-C.; Lu, T.-M. *Proc. SPIE* **2003**, *5219*, 59–73.
- (31) Steele, J.; Brett, M. J. *Mater. Sci.: Mater. Electron.* **2007**, *18*, 367–379.
- (32) Barkocy-Gallagher, G. A.; Arthur, T. M.; Siragusa, G. R.; Keen, J. E.; Elder, R. O.; Laegreid, W. W.; Koohmaraie, M. *Appl. Environ. Microbiol.* **2001**, *67*, 3810–3818.
- (33) Harmon, B. G.; Brown, C. A.; Tkalcic, S.; Mueller, P. O. E.; Parks, A.; Jain, A. V.; Zhao, T.; Doyle, M. P. *J. Food Prot.* **1999**, *62*, 574–579.
- (34) Tkalcic, S.; Zhao, T.; Harmon, B. G.; Doyle, M. P.; Brown, C. A.; Zhao, P. J. *J. Food Prot.* **2003**, *66*, 1184–1189.
- (35) Hodgkinson, I.; Wu, Q. H.; Hazel, J. *Appl. Opt.* **1998**, *37*, 2653–2659.
- (36) Tait, R. N.; Smy, T.; Brett, M. J. *Thin Solid Films* **1993**, *226*, 196–201.
- (37) Tanto, B.; Ten Eyck, G.; Lu, T. M. *J. Appl. Phys.* **2010**, *108*, 026107.
- (38) Groza, J. R. *Nanostruct. Mater.* **1999**, *12*, 987–992.
- (39) Wen, X.; Wang, S.; Ding, Y.; Wang, Z. L.; Yang, S. J. *Phys. Chem. B* **2005**, *109*, 215–220.
- (40) Demianets, L. N.; Pouchko, S. V.; Gaynutdinov, R. V. *J. Cryst. Growth* **2003**, *259*, 165–178.
- (41) Ferraz, L. C. C.; Carvalho, W. M.; Criado, D.; Souza, F. L. *ACS Appl. Mater. Interfaces* **2012**, *4*, 5515–5523.
- (42) Cornuz, M.; Grätzel, M.; Sivula, K. *Chem. Vap. Deposition* **2010**, *16*, 291–295.
- (43) Li, L.; Koshizaki, N. *J. Mater. Chem.* **2010**, *20*, 2972–2978.
- (44) Bersani, D.; Lottici, P.; Montenero, A. *J. Raman Spectrosc.* **1999**, *30*, 355–360.
- (45) McCarty, K. F. *Solid State Commun.* **1988**, *68*, 799–802.
- (46) Martin, T.; Meerlin, R.; Huffman, D.; Cardona, M. *Solid State Commun.* **1977**, *22*, 565–567.
- (47) Manificier, J.; Gasiot, J.; Fillard, J. *J. Phys. E: Sci. Instrum.* **2001**, *9*, 1002.
- (48) Yoldas, B. E.; Partlow, D. P. *Thin Solid Films* **1985**, *129*, 1–14.
- (49) Lethy, K. J.; Beena, D.; Pillai, V. P. M.; Ganesan, V. *J. Appl. Phys.* **2008**, *104*, 033515.
- (50) Akl, A. A. *Appl. Surf. Sci.* **2004**, *233*, 307–319.
- (51) Zhang, Z.; Hossain, M. F.; Takahashi, T. *Appl. Catal., B* **2010**, *95*, 423–429.
- (52) Zhang, G.-Y.; Feng, Y.; Xu, Y.-Y.; Gao, D.-Z.; Sun, Y.-Q. *Mater. Res. Bull.* **2012**, *47*, 625–630.
- (53) Kay, A.; Cesar, I.; Grätzel, M. *J. Am. Chem. Soc.* **2006**, *128*, 15714–15721.
- (54) Gao, Q.-X.; Wang, X.-F.; Di, J.-L.; Wu, X.-C.; Tao, Y.-R. *Catal. Sci. Technol.* **2011**, *1*, 574–577.
- (55) Liu, X.; Liu, J.; Chang, Z.; Sun, X.; Li, Y. *Catal. Commun.* **2011**, *12*, 530–534.
- (56) Zheng, Y.; Cheng, Y.; Wang, Y.; Bao, F.; Zhou, L.; Wei, X.; Zhang, Y.; Zheng, Q. *J. Phys. Chem. B* **2006**, *110*, 3093–3097.
- (57) Reddy, B. V.; Rasouli, F.; Hajaligol, M. R.; Khanna, S. N. *Fuel* **2004**, *83*, 1537–1541.
- (58) Weiss, W.; Ranke, W. *Prog. Surf. Sci.* **2002**, *70*, 1–151.
- (59) Zhou, X.; Lan, J.; Liu, G.; Deng, K.; Yang, Y.; Nie, G.; Yu, J.; Zhi, L. *Angew. Chem., Int. Ed.* **2012**, *51*, 178–182.
- (60) Hardee, K. L.; Bard, A. J. *J. Electrochem. Soc.* **1977**, *124*, 215–224.
- (61) Miyauchi, M.; Nakajima, A.; Watanabe, T.; Hashimoto, K. *Chem. Mater.* **2002**, *14*, 2812–2816.
- (62) Chawengkijwanich, C.; Hayata, Y. *Int. J. Food Microbiol.* **2008**, *123*, 288–292.
- (63) Foster, H. A.; Sheel, D. W.; Sheel, P.; Evans, P.; Varghese, S.; Rutschke, N.; Yates, H. M. *J. Photochem. Photobiol. A* **2010**, *216*, 283–289.
- (64) Qiu, X.; Miyauchi, M.; Sunada, K.; Minoshima, M.; Liu, M.; Lu, Y.; Li, D.; Shimodaira, Y.; Hosogi, Y.; Kuroda, Y.; Hashimoto, K. *ACS Nano* **2011**, *6*, 1609–1618.
- (65) Dunnill, C. W.; Ansari, Z.; Kafizas, A.; Perni, S.; Morgan, D. J.; Wilson, M.; Parkin, I. P. *J. Mater. Chem.* **2011**, *21*, 11854–11861.
- (66) Chen, Y.; Lu, A.; Li, Y.; Zhang, L.; Yip, H. Y.; Zhao, H.; An, T.; Wong, P. K. *Environ. Sci. Technol.* **2011**, *45*, 5689–5695.
- (67) Wang, W.; Yu, Y.; An, T.; Li, G.; Yip, H. Y.; Yu, J. C.; Wong, P. K. *Environ. Sci. Technol.* **2012**, *46*, 4599.
- (68) Wei, C.; Lin, W. Y.; Zainal, Z.; Williams, N. E.; Zhu, K.; Kruzic, A. P.; Smith, R. L.; Rajeshwar, K. *Environ. Sci. Technol.* **1994**, *28*, 934–938.
- (69) Horie, Y.; David, D. A.; Taya, M.; Tone, S. *Ind. Eng. Chem. Res.* **1996**, *35*, 3920–3926.
- (70) Koizumi, Y.; Taya, M. *Biochem. Eng. J.* **2002**, *12*, 107–116.
- (71) Sun, D. D.; Tay, J. H.; Tan, K. M. *Water Res.* **2003**, *37*, 3452–3462.
- (72) Keller, E. F.; Segel, L. A. *J. Theor. Biol.* **1971**, *30*, 225–234.
- (73) Lewus, P.; Ford, R. M. *Biotechnol. Bioeng.* **2001**, *75*, 292–304.
- (74) Gogniat, G.; Thyssen, M.; Denis, M.; Pulgarin, C.; Dukan, S. *FEMS Microbiol. Lett.* **2006**, *258*, 18–24.
- (75) Bos, R.; van der Mei, H. C.; Busscher, H. J. *FEMS Microbiol. Rev.* **1999**, *23*, 179–230.
- (76) Emerson; Bergstrom, T. S.; Liu, Y.; Soto, E. R.; Brown, C. A.; McGimpsey, W. G.; Camesano, T. A. *Langmuir* **2006**, *22*, 11311–11321.